CONF-901101--30

Paper to be presented to the ANS Winter Meeting Session
on Thermal Hydraulics of Severe Accidents,
Washington, D.C., November 11-15, 1990

CONF-901101--30

DE90 017695

THE MELTSPREAD-1 COMPUTER CODE FOR THE ANALYSIS OF TRANSIENT SPREADING IN CONTAINMENTS

by

M. T. Farmer, J. J. Sienicki, and B. W. Spencer

Reactor Analysis and Safety Division
Argonne National Laboratory
9700 S. Cass Avenue
Argonne, IL 60439

Work sponsored by the Electric Power Research Institute, Palo Alto, CA, under Contract RP 3047-2.

THE MELTSPREAD-1 COMPUTER CODE FOR THE ANALYSIS OF TRANSIENT SPREADING IN CONTAINMENTS

M. T. Farmer, J. J. Sienicki, and B. W. Spencer
Argonne National Laboratory
9700 S. Cass Avenue, Argonne, IL 60439 (708) 972-4539

ABSTRACT

A one-dimensional, multicell, Eulerian finite difference computer code (MELTSPREAD-1) has been developed to provide an improved prediction of the gravity driven spreading and thermal interactions of molten corium flowing over a concrete or steel surface. In this paper, the modeling incorporated into the code is described and the spreading models are benchmarked against a simple "dam break" problem as well as water simulant spreading data obtained in a scaled apparatus of the Mk I containment. Results are also presented for a scoping calculation of the spreading behavior and shell thermal response in the full scale Mk I system following vessel meltthrough.

NOMENCLATURE

D	-	hydraulic diameter of spreading corium layer, m
e	-	specific enthalpy, J/kg
$e_{ablation}$	-	ablating substrate specific enthalpy at solidus, J/Kg
e_{crust}	-	crust specific enthalpy at solidus, J/Kg
Δe_f	-	crust latent heat of fusion, J/Kg
Δe^i_{dc}	-	concrete decomposition enthalpy, J/Kg
E	-	relative substrate elevation, m
f_{fric}	-	friction factor
F_{CO_2}	-	reaction fraction of CO_2 gas sparging through melt layer
F_{H_2O}	-	reaction fraction of H_2O vapor sparging through melt layer
g	-	gravitational acceleration, m^2/s
h	-	collapsed depth of melt layer, m
h_{bot}	-	heat transfer coefficient at bottom surface, $W/m^2.K$
h_{top}	-	heat transfer coefficient at top surface, $W/m^2.K$
h_{conv}	-	forced convection heat transfer coefficient, $W/m^2.K$
k	-	thermal conductivity, W/m.K
$\dot{m}_{H_2O}$	-	mass flux of H_2O vapor due to concrete decomposition in substrate, $Kg/m^2.s$
$\dot{m}_{CO_2}$	-	mass flux of CO_2 gas due to concrete decomposition in substrate, $kg/m^2.s$
$\dot{m}_{vessel}$	-	mass flux of corium from reactor pressure vessel $kg/m^2.s$
Pr	-	Prandtl number
q^i_{ox,H_2O}	-	oxidation energy release for reaction of i^{th} melt constituent with H_2O vapor, J/kg
q^i_{ox,CO_2}	-	oxidation energy release for reaction of i^{th} melt constituent with CO_2 vapor, J/kg
$\dot{q}_{decay}$	-	decay heat generation rate per unit mass of UO_2, W/kg
Re	-	Reynolds number
S	-	perimeter length normal to flow, m
t	-	time, s
T	-	temperature, K
T_{bot}	-	surface temperature at bottom of corium layer, K
T_{top}	-	surface temperature at top of corium layer, K
U	-	velocity, m/s
$x^i_{surface}$	-	weight fraction of i^{th} melt constituent in solidified debris
x^i_{melt}	-	weight fraction of i^{th} melt constituent in molten corium
x^i_{vessel}	-	weight fraction of i^{th} melt constituent draining from reactor pressure vessel
y	-	coordinate normal to substrate surface, m
z	-	coordinate parallel to substrate surface, m

Greek Symbols

α	=	void fraction
δ	=	crust thickness, m
η	=	thickness of eroded substrate, m
σ	=	corium surface tension, N/m
ρ	=	density, kg/m^3
μ	=	viscosity, kg/m.s

Superscripts

i	=	corium constituent

Subscripts

l	=	value at liquidus
s	=	value at solidus
surface	=	value at surface of substrate
shell	=	value at shell surface

INTRODUCTION

For Mk I Boiling Water Reactor severe accident sequences in which molten corium is postulated to melt through the reactor pressure vessel lower head, a significant question concerns the potential for corium to spread over the drywell floor and cause early failure of the containment shell. Figure 1 illustrates the pedestal and drywell regions in the Peach Bottom Mk I system. The reinforced concrete pedestal walls represent an initial barrier to the spreading corium. However, corium which collects on the pedestal floor is generally free to flow out the personnel access doorway into the surrounding drywell region. A major question is then whether the spreading corium is able to propagate to the shell where the associated thermal loading might lead to early containment shell failure, or whether heat transfer to structure, underlying concrete, and overlying water will freeze and immobilize the melt short of the shell thus precluding damaging thermal attack.

Several experimental and analytical research efforts on corium spreading potential and shell attack have been reported in the literature. Predictions of shell meltthrough were first performed by Greene et al.[1] using corium conditions obtained from CORCON calculations of the molten core concrete interaction (MCCI) following the assumed uniform spreading of a large corium mass over the pedestal and drywell regions. Estimates of corium lateral migration associated with long-term MCCI were performed by Corradini[2] for the case of gradual corium addition to the MCCI zone. For this case, lateral relocation of corium occurs as a result of sidewards and downwards concrete ablation as calculated with a modified version of the CORCON code. Kazimi[3] estimated the corium spreading potential assuming that spreading takes place in a semi-circular region and that the heat transfer coefficient is characeristic of non-spreading, natural convective MCCI's. Greene[4] conducted simulant spreading experiments in which molten lead jets were impinged upon plywood, marble, and steel non-reactive surfaces both with and without the presence of an initial water layer on the surface. Based on the results of his experiments, Greene developed a correlation for the mean melt spreading thickness in terms of the melt pour volume, depth of the water pool, latent and sensible heat content of the impinging melt, and latent heat of vaporization of the water pool. However, no information on time dependent melt or pour conditions and spreading front propagation has yet been made available for these experiments. Henry[5] conducted simulant experiments in which iron-alumina thermite was injected into a steel-walled linear flow channel containing two rectalinear compartments and a concrete base to investigate quenching of debris which has spread over concrete and come to rest against a vertical steel wall.

Recently, Theofanous et al.[6] conducted simulant spreading experiments using water in a 1/10 linear scale model of the MK I containment. Water heights as a function of time at various locations in the pedestal and drywell regions were measured. Based on the results of their scaled experiments, Theofanous et al. concluded that the flow characteristics in the drywell are controlled by the driving gravity head across the pedestal doorway.

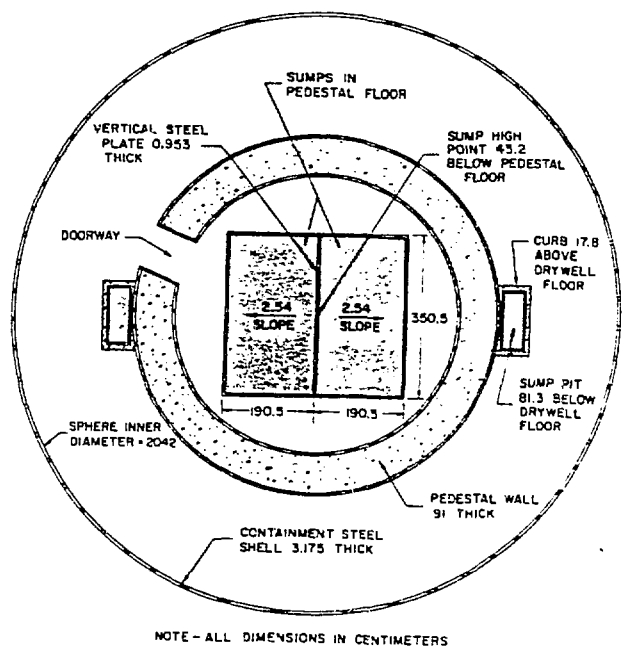

Figure 1. Illustration of Mk I Drywell Configuration (Peach Bottom Units 2 and 3).

The development of a computational capability to provide an analysis framework for the assessment of spreading potential and the associated shell thermal loading in Mk I containments was undertaken at Argonne National Laboratory. The initial version of a transient spreading model was the MELTSPREAD-0 code developed by Sienicki, et al.[7,8] This code assumed quasi-steady concrete ablation and did not account for melt freezing, immobilization, and subsequent flow over the solidified leading edge. MELTSPREAD-0 was applied to analyze the iron-alumina thermite spreading experiments of Henry.[5] In these experiments, the thermite injection time was short in comparison to the time for the melt to spread the length of the channel.[5] Therefore, in the analysis it was assumed that the thermite was instantaneously deposited in the injection compartment and, thereafer, relocated in a 1-D spreading trough under the influence of gravity. Model predictions indicated that the thermite would spread the full length of the channel without freezing at the leading edge, which is in agreement with the experiment observations. MELTSPREAD-0 was also used to perform scoping calculations of the flow out of the pedestal doorway in the full-scale Mk I system. These calculations indicated that for a 25 K initial melt superheat, the corium leading edge would begin to freeze midway between the pedestal doorway and the shell. For an initial superheat of 250 K, the corium was predicted to reach the shell with a non-negligible amount of melt superheat. In these calculations, in-pedestal energy losses from the relocating melt were not considered.

Development of a transient spreading model is continuing in the form of the MELTSPREAD-1 code. MELTSPREAD-1 contains more detailed models for the processes treated in MELTSPREAD-0 as well as many new models for phenomena that were ignored in the earlier code. MELTSPREAD-1 currently accounts for: gravity-driven flow both in-pedestal and ex-pedestal; melt freezing, immobilization, and remelting; concrete heatup, decomposition, and gas release; concrete melting and ablation; enhancement of heat transfer to overlying water or underlying concrete due to sparging decomposition gases; chemical oxidation of melt metallic constituents; spreading of melt over previously spread material; and two-dimensional heatup of the shell due to forced convection and impingement heat transfer from spreading melt adjacent to the shell.

The present paper provides a summary of the models incorporated into the MELTSPREAD-1 code, a benchmark calculation of the melt relocation model against a simple "dam break" problem, and a comparison of the spreading model with the simulant spreading data obtained by Theofanous in a scaled Mk I containment apparatus. In addition, the results of scoping calculations of the predicted spreading behavior for the full scale Mk I system with water present in the cavity are provided.

MODEL DEVELOPMENT

A depiction of the corium spreading process over a concrete surface in the presence of water is provided in Figure 2. The relocation model incorporated into MELTSPREAD-1 performs a fluid

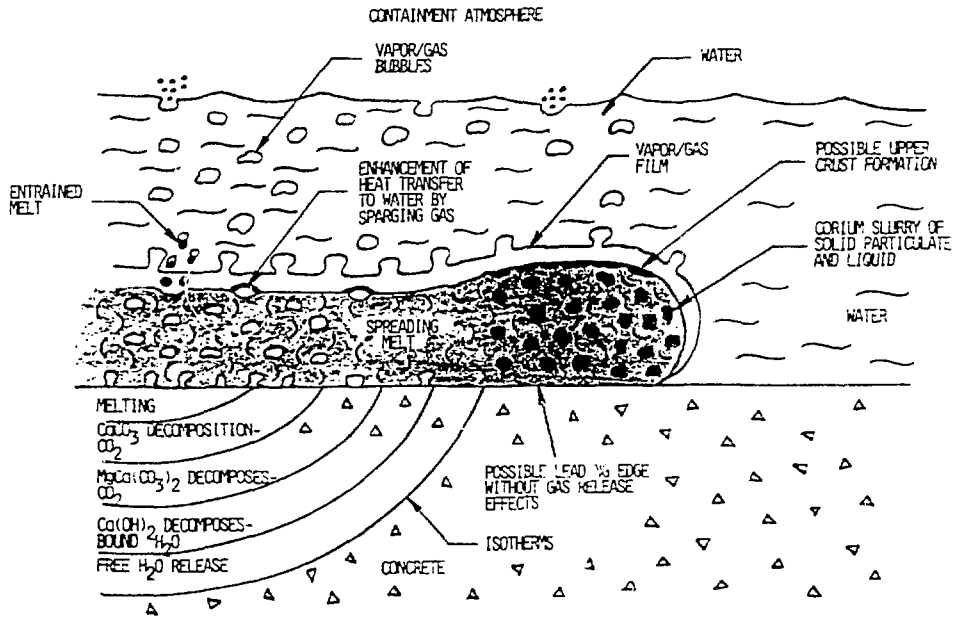

Figure 2. Depiction of Corium Spreading Process over Concrete.

dynamics calculation of the gravity-driven motions of a molten mass spreading in a one-dimensional flow channel of varying cross-sectional area. The fluid velocity is assumed to satisfy the equation,

$$\frac{\partial U}{\partial t} + \frac{1}{2}\frac{\partial U^2}{\partial z} = -\frac{1}{2} g \frac{\partial}{\partial z}\left[\frac{h}{1-\alpha} + E\right] - \frac{4\tau}{\rho D}, \qquad (1)$$

where

$$D = \frac{4h}{1-\alpha}, \qquad (2)$$

$$\tau = \frac{1}{2} \rho U|U| f_{fric}. \qquad (3)$$

The nonconservative form of the momentum equation is employed because it reduces to Bernoulli's law in the limit of frictionless flow. The friction factor is calculated using the correlation of Colebrook and White.[9] The hydrostatic pressure gradient is based on the melt height plus the basemat elevation. The local melt void fraction due to concrete decomposition gases sparging through the melt is calculated based on the correlation of Kataoka and Ishii.[10] The elevation gradient is included to account for the presence of previously solidified debris and the profile of the initial spreading surface such as the presence of a sump pit. Spreading is restricted to occur such that the melt depth at the leading edge does not fall below the minimum depth at which surface tension balances gravity,

$$h_{min} = \sqrt{\frac{2\sigma}{g\rho}}. \qquad (4)$$

The collapsed depth, h, in Eq. (1) is written as a sum of the local melt constituent collapsed depths, h^i. MELTSPREAD-1 tracks a total of 16 melt constituents, which include Zr, Cr, Fe, Ni, B_4C, U, C, B, FeO, Fe_2O_3, Fe_3O_4, ZrO_2, Cr_2O_3, NiO, UO_2, B_2O_3, and slag. The metals are treated as a distinct phase from the oxides. The conservation of mass equation for the i^{th} melt constituent is as follows:

$$S\frac{\partial}{\partial t}(\rho^i h^i) + \frac{\partial}{\partial z}(S\rho^i h^i U) - \beta^i S\left[F_{H_2O}\gamma^i_{H_2O}\dot{m}_{H_2O} + F_{CO_2}\gamma^i_{CO_2}\dot{m}_{CO_2}\right] + S\frac{\rho^i_s}{\rho^i_l}\left[x^i_{surface}\frac{d\eta}{dt} - x^i_{melt}\frac{d\delta}{dt}\right] + S\,x^i_{vessel}\dot{m}_{vessel} \qquad (5)$$

where

$$\beta^i = \begin{cases} +1, & \text{oxidizable melt constituents} \\ -1, & \text{oxidized melt constituents} \\ 0, & \text{non-oxidizable and non-oxidized melt constituents.} \end{cases} \qquad (6)$$

The third term in Eq. (5) accounts for oxidation in the melt layer. Carbon dioxide and water vapor arising from concrete decomposition are assumed to react with zirconium, chromium, and iron. The oxidation fractions, F_{H_2O} and F_{CO_2} account for incomplete reaction of the sparging gases as the gas bubbles rise through the melt layer; these functions are calculated based on transient diffusion theory.[11] $\gamma^i_{H_2O}$ and $\gamma^i_{CO_2}$ are stoichiometric constants. For the oxidation of zirconium,

$$\gamma^{Zr}_{H_2O} = M_{Zr}/2M_{H_2O} \text{ and } \gamma^{Zr}_{CO_2} = M_{Zr}/2M_{CO_2}.$$

Depending on the melt-substrate interfacial boundary condition, the fourth term in Eq. (5) accounts for mass transfer due to substrate ablation and/or crust formation. The sixth term in Eq. (5) accounts for local, time-dependent mass addition to the melt layer due to drainage from the reactor pressure vessel. As depicted in Figure 3, a significant amount of below vessel structure exists in the form of control rod drive and instrument tube housings, in addition to a personnel catwalk. Corium draining from a localized breach in the reactor pressure vessel may undergo significant splashing as it passes

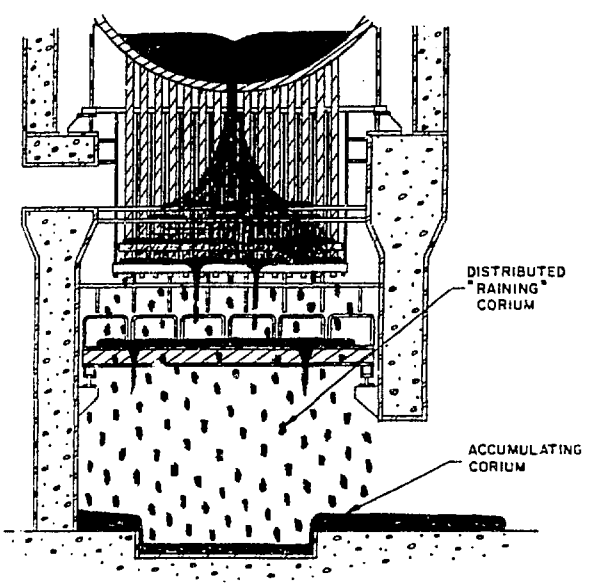

Figure 3. Depiction of Corium Interaction with Below Vessel Structure.

through this structure, thus causing the corium to "rain" down on the pedestal floor. To account for this behavior, MELTSPREAD-1 permits melt addition to the spreading layer over a distributed area as well as a localized area.

The spreading melt constituents are assumed to be in local thermodynamic equilibrium at a single, local layer specific enthalpy. The enthalpy is obtained from the solution of the energy conservation equation,

$$S\frac{\partial}{\partial t}(\rho he) + \frac{\partial}{\partial z}(S\rho heU) =$$
$$- Sh_{bot}(T-T_{bot}) \quad Sh_{top}(T-T_{top})$$
$$+ S\rho\dot{h}q_{decay} + S\dot{m}_{vessel}e_{vessel}$$
$$+ S\rho\left[e_{ablation}\frac{d\eta}{dt} - e_{crust}\frac{d\delta}{dt}\right]$$
$$+ SF_{H_2O}\dot{m}_{H_2O}\sum_i \gamma^i_{H_2O}\, q^i_{ox,H_2O}$$
$$+ SF_{CO_2}\dot{m}_{CO_2}\Sigma\gamma^i_{CO_2}\, q^i_{ox,CO_2}. \qquad (7)$$

The local enthalpy in the melt layer is checked to determine if the enthalpy has fallen below the solidus value. If so, the melt is immobilized and added to previously solidified melt and concrete in the calculation. If the enthalpy lies between the liquidus and solidus, the melt is modeled as a slurry with enhanced effective viscosity as given by the correlation of Ishii and Zuber,[12]

$$\mu_{slurry} = \frac{\mu}{\left(1 - \frac{\alpha_{solid}}{\alpha_{solid} + \alpha_{liquid}}\right)^{2.5}}. \qquad (8)$$

At the melt lower surface, a variety of boundary conditions are treated to encompass a range of melt-substrate interaction conditions. These boundary conditions include: (1) a growing stable crust upon solid substrate, (2) thin crust segments upon a solid substrate, (3) substrate ablation with a growing stable crust, (4) substrate ablation without a crust, (5) substrate melting without removal of melt beneath a growing crust, and (6) a solid substrate without crust formation. For the cases of stable crust growth, the crust depth satisfies the equation,

$$\rho\Delta e_f\frac{d\delta}{dt} = k\left.\frac{\partial T}{\partial y}\right|_{y=\delta}$$
$$- h_{bot}(T - T_{solidus}). \qquad (9)$$

A current source of uncertainty is the applicable heat transfer coefficients at the melt upper and lower surfaces during corium spreading. At the lower surface, the heat transfer coefficient options include: (1) forced convection, (2) bubble agitation, or (3) sum of forced convection and bubble agitation models. The forced convection heat transfer coefficient is assumed to be given by the fully developed pipe flow expression,

$$h_{conv} = \begin{cases} 7.6\frac{k}{D}; & Re < 2300 \\ 0.023\, Re^{0.8}\, Pr^{0.4}\frac{k}{D}; & Re \geq 2300 \end{cases} \qquad (10)$$

where the Reynolds number is based on the melt hydraulic diameter as defined in Eq. (2). The bubble-agitation heat transfer coefficient is calculated using the periodic contact model of Kao and Kazimi.[13]

At the melt upper surface, MELTSPREAD-1 treats heat transfer to either an overlying water layer or heat transfer to a dry atmosphere. Additionally, crusting may be assumed to be absent at the upper surface, or the heat transfer may be assumed to be limited by thin crust segments which move with the melt layer. If water is absent, the heat transfer coefficient is calculated assuming radiation off the top of the melt. If water is present, the heat transfer is calculated along the full boiling curve. Heat transfer in the nucleate boiling regime is calculated using Rohsenow's correlation.[14] The critical heat flux is calculated using Zuber's model[15] with a correction for subcooling due to Ivey-Morris.[16] In the film boiling regime, the melt-to-water heat transfer is calculated using the CORQUENCH model,[17] which accounts for radiant heat transfer across the film, noncondensable gases, bulk liquid subcooling, melt-water interfacial area enhancement due to sparging gas, and melt entrainment into the overlying water layer. The minimum film boiling temperature is calculated using Henry's correlation.[18] In the transition boiling regime, a linear variation between the critical heat flux and the minimum film boiling heat flux is assumed.

When water is present, MELTSPREAD-1 performs a local check on the height of the melt layer relative to the downcomer height above the drywell floor. In Mk I containments, the downcomers limit the water height in the pedestal and drywell regions by allowing for spillover into the steam suppression pool. If the melt height exceeds the downcomer height, a radiation boundary condition is applied at the melt upper surface.

In the underlying substrate, MELTSPREAD-1 solves a one-dimensional transient heat conduction equation to obtain the local substrate enthalpy,

$$\rho \frac{\partial e}{\partial t} = \frac{\partial}{\partial y}\left[k \frac{\partial T}{\partial y}\right] + \rho \dot{q}_{decay}. \quad (11)$$

Equation (11) is applied to both concrete and steel substrates, as well as solidified debris. The concrete property routines incorporated into MELTSPREAD-1 implicitly account for the decomposition enthalpies associated with the generation of water vapor (evaporable H_2O and decomposition of $Ca(OH)_2$), and the generation of carbon dioxide (decomposition of $CaCO_3$ and $MgCa(CO_3)_2$). The front locations for each of these decomposition processes satisfies the equation,

$$\rho \Delta e^{i}_{dc} \frac{dy^{i}}{dt}_{front} = - k \frac{\partial T}{\partial y}\Big|_{y^{i}_{front}+\epsilon} + k \frac{\partial T}{\partial y}\Big|_{y^{i}_{front}-\epsilon}. \quad (12)$$

The concrete degassing rate for evaporable H_2O is therefore,

$$\dot{m}_{bound\ H_2O} = x_{bound\ H_2O}\ \rho \frac{dy}{dt}_{bound\ H_2O}. \quad (13)$$

Similar expressions apply to the decomposition of $Ca(OH)_2$, $CaCO_3$, and $MgCa(CO_3)_2$. The decomposition temperatures assumed in MELTSPREAD-1 are the system saturation temperature for evaporable H_2O, 853 K for $Ca(OH)_2$, 1000 K for $MgCa(CO_3)_2$, and 1098 K for $CaCO_3$. The maximum enthalpy obtained by the concrete is monitored such that the correct degassing rate is predicted upon reheating of concrete which has undergone quenching following the onset of decomposition.

If the melt propagates to the shell, MELTSPREAD-1 invokes a two-dimensional transient heatup calculation. The physical situation is depicted in Figure 4. The governing equation for the shell heatup calculation is of the form,

$$\rho \frac{\partial e}{\partial t} = \frac{\partial}{\partial x}\left(k \frac{\partial T}{\partial x}\right) + \frac{\partial}{\partial y}\left(k \frac{\partial T}{\partial y}\right). \quad (14)$$

If the shell surface temperature lies below the melt freezing temperature, stable crust growth on the shell is calculated according to the equation,

$$\rho \Delta e_f \frac{d\delta}{dt} = k \frac{\partial T}{\partial y}_{y=\delta} - h_{shell}\,(T - T_{solidus}). \quad (15)$$

The convective heat transfer coefficient between the shell and melt is currently modeled using a jet impingement heat transfer correlation,[19]

$$h_{shell} = .00\,Re^{0.8}\,Pr^{1/3}\,\frac{k}{D}$$

where the Reynolds number is based on the voided melt depth and on the melt velocity impinging upon the shell.

If water is absent, the heat transfer from the shell surface above the melt layer is calculated using a radiation heat transfer coefficient. Heating of the shell above the melt due to radiation from the melt adjacent to the shell is currently not modeled. If water is present, the heat transfer is calculated along a full boiling curve. Heat transfer in the nucleate boiling regime is again calculated using Rohsenow's equation[14] with a correction for shell inclination according to the correlation of Jung et al.[20] The critical heat flux is assumed to be given by Zuber's model.[15] The minimum film boiling temperature is calculated using Henry's correlation.[18] The film boiling heat transfer coefficient is calculated using Berenson's model[21] with a correction for shell inclination according to the experimental results of Sauer et al.[22]

An implicit finite difference numerical scheme is employed to solve the above system of equations. A depiction of the nodalization scheme for the Mk I system is shown in Figure 5. In-pedestal, the flow is assumed to occur in a 360° sector. Through the pedestal doorway, the flow is assumed to occur in a one-dimensional channel. In the drywell annulus between the doorway and shell, the flow is assumed to occur in a 90° sector (the choice of flow angle is arbitrary). Thereafter, the melt is assumed to

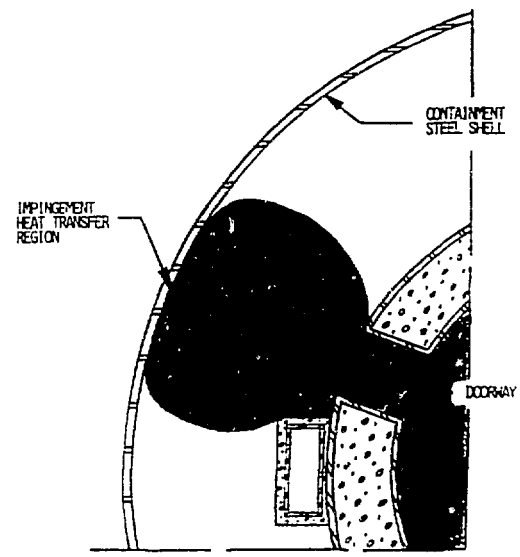

Figure 4. Depiction of Corium Interaction with Shell.

spill over into the balance of the drywell annulus, which is modelled as a one-dimensional spreading channel of width equal to twice the distance between the drywell shell and the outside of the pedestal wall.

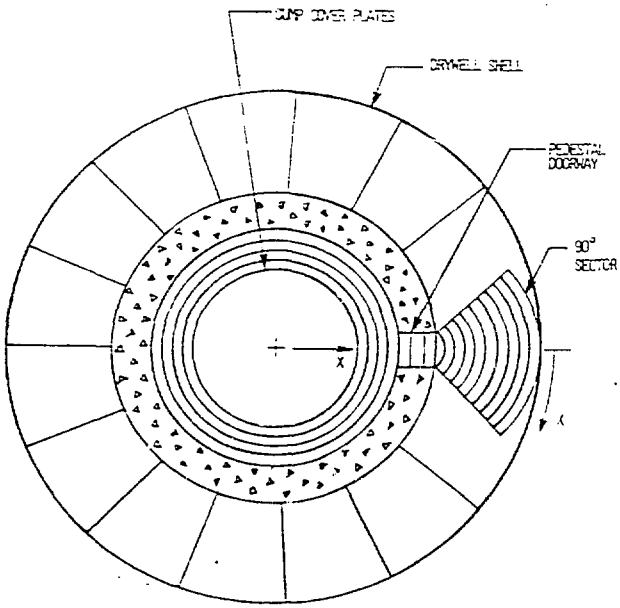

Figure 5. Depiction of Nodalization Scheme for Mk I Containments.

COMPARISON WITH DAM BREAK ANALYTICAL SOLUTION

An important part of MELTSPREAD development has been comparison with relevant analytical solutions and experiment data. MELTSPREAD-0 was previously compared with the FAI thermite tests.[7] Since the ultimate spreading penetration in those experiments was predicted to be limited by the short length of the test section channel, the results of that comparison are also valid for MELTSPREAD-1 which would provide similar predictions.

In order to test the hydrodynamics modeling in MELTSPREAD-1, the code has been compared to the analytical solution for a one-dimensional "dam break" problem. Since this problem contains no heat transfer effects, the heat transfer models in the code were bypassed. Of principal interest is whether correct spreading depths and velocities are calculated. The particular example calculated is a 20 m long flow channel initially filled to a uniform depth of 10 cm over half the length of the channel. At zero time, the "dam" barrier is removed and the fluid is allowed to relocate under the influence of gravity. According to gravity current theory,[23] after short term transient effects have died away, the advancing front will obtain a depth equal to one half the initial fluid depth, and (in an Eulerian coordinate system) the advancing and receding wave fronts will achieve a velocity equal to $\frac{1}{2}\sqrt{dg}$, where d = the initial water depth in the channel. For the example, then, the fronts should propagate with a velocity of 0.5 m/sec.

The predicted height distributions at selected times calculated with MELTSPREAD-1 are shown in Figure 6, while the advancing and receding front propagation distances (measured from the original dam location) are presented in Figure 7. The front distances are obtained by tracking the 2.5 cm (advancing front) and 7.5 cm (receding front) heights. As is evident from Figure 6, the model slightly underpredicts the theoretical advancing front depth of 5 cm throughout the calculated time domain. Examination of Figure 7 indicates that the calculated advancing and receding front propagation distances are predicted to within 6 percent. Thus, the hydrodynamics modeling in MELTSPREAD-1 correctly predicts the gravity-driven spreading behavior in the dam break problem to within a suitable tolerance.

COMPARISON WITH WATER SPREADING EXPERIMENTS

There is currently a lack of experiment data using prototypic materials in a scaled Mk I apparatus. The only available spreading data in a Mk I is the water simulant data of Theofanous et al.[6]

Given that MELTSPREAD-1 predicts the correct spreading depths and front velocities for the dam break problem, the model was applied to predict the relocation behavior of water in the more complex, scaled Mark I geometry employed by Theofanous et al.[6] The apparatus was an approximate 1/10 linear scale model of the Peach Bottom pedestal and drywell depicted in Figure 1. The assumed dimensions for the scaled experiment are as follows: pedestal inner radius = 28.3 cm, pedestal wall thickness = 0.3 cm, shell radius = 56.5 cm, and pedestal doorway width = 9.5 cm. Transient depth profiles within the apparatus were measured at five locations: location A, just inside the pedestal doorway; location B, just outside the pedestal doorway; location C, adjacent to the shell across from the doorway; location D, in the annulus 90° from the doorway; and location E, in the annulus diametrically opposite of the doorway.

Theofanous et al. reasoned that the ex-pedestal flow would be controlled by the gravity head across the pedestal doorway.[6] Accordingly, pour conditions were scaled based on conservation of the Froude number. For the 1/10 scale experiment, Theofanous et al. concluded that the pour times scale as 1/3 and pour rates scale as 3/1000. In order to avoid experiment distortions due to capillary effects, Theofanous et al.

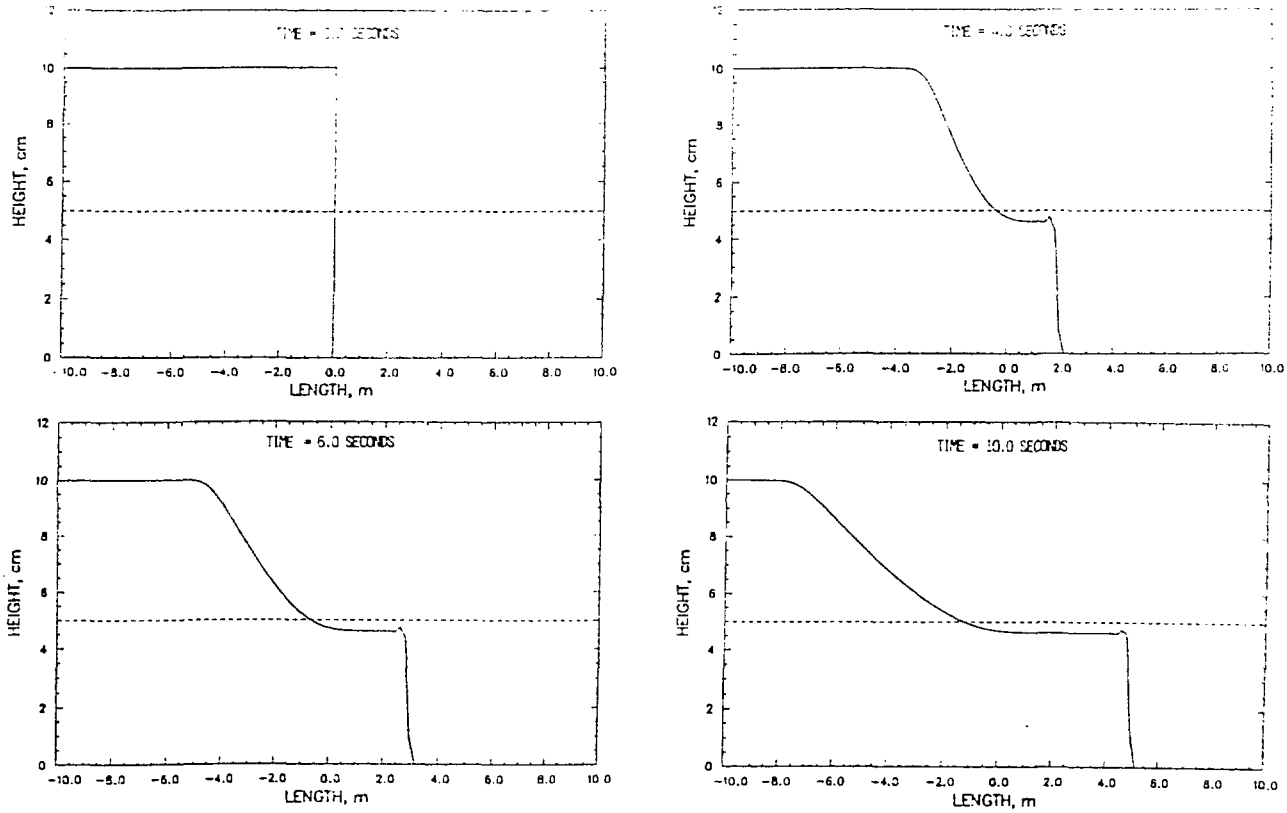

Figure 6. Predicted Height Distributions as a Function of Time for the Dam Break Problem.

considered only high flowrate pours as typically predicted by MAAP code calculations. Transient height profiles for two runs were reported. Run No. 1 was a 1/10 scale simulation of 10 m^3 pour volume at a pour rate of 6.5 m^3/min. The corresponding pour rate in the scaled experiment was reported to be constant at 19.5 liters/min.[6] Run No. 2 considered the same pour volume at reactor scale, but the pour rate was reduced to 3.25 m^3/min. The corresponding pour rate in the scaled experiment for this case was reported to be constant at 9.75 liters/min. Calculations were performed for both of the reported tests.

The predicted transient height profiles for Run No. 2 at selected times are shown in Figure 8. The coordinate system for the length in these figures is illustrated in Figure 5. A comparison of the predicted height transients with the experimental data obtained at Locations A, C, D, and E is shown in Figure 9. Data for Location B were not presented in Reference 6. Examination of Figure 9 indicates that the arrival time at locations A and C are reasonably predicted, whereas the arrival times at locations D and E are slightly underpredicted. No estimate of the experimental error associated with the measured height profiles was provided in Reference 6, and therefore it is not possible to determine whether the descrepancy in arrival times lies outside the range of uncertainty associated with the experiment.

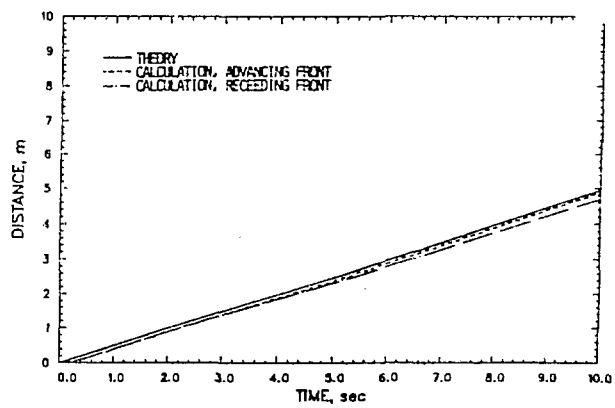

Figure 7. Comparison of Predicted Advancing and Receding Front Distances with Analytical Solution.

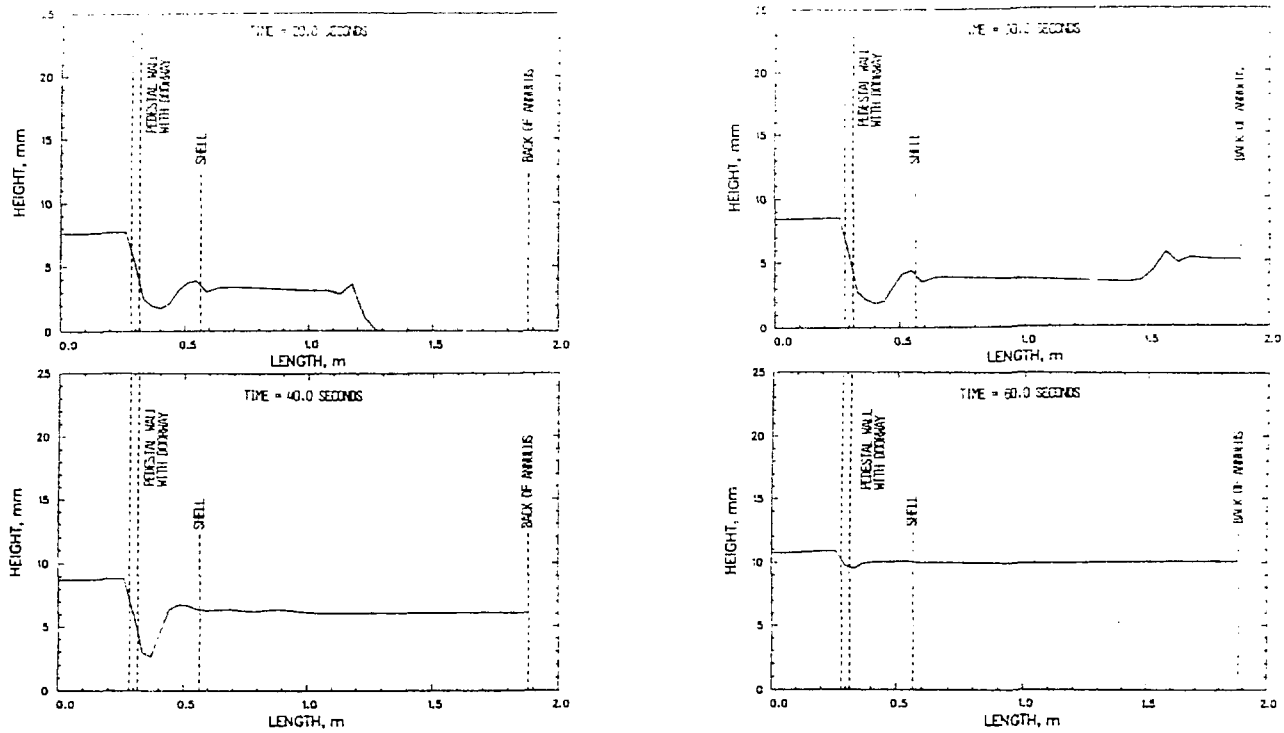

Figure 8. Predicted Height Distributions at Various Times for Run No.2 of the Experiment of Theofanous et al.[6]

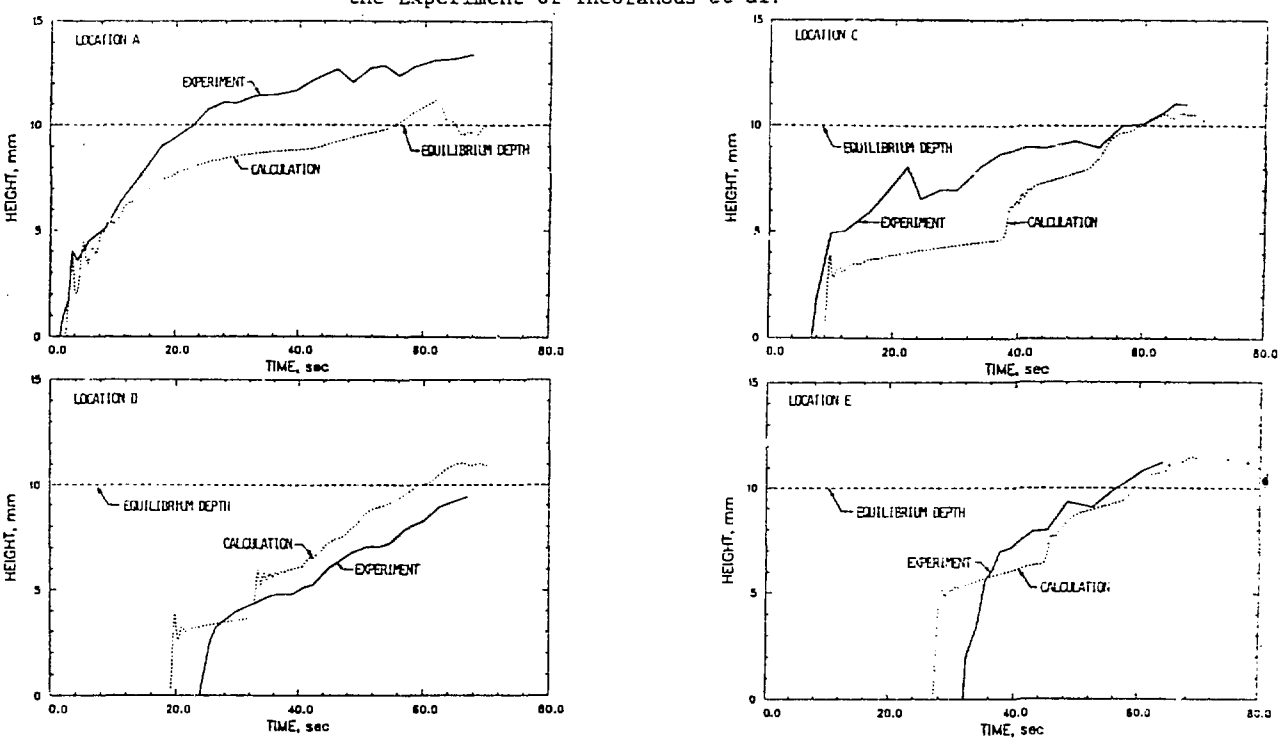

Figure 9. Comparison of Predicted Height Transients with the Experimental Data of Theofanous et al.[6] for Run No. 2 at Locations A, C, D, and E.

For location A, the in-pedestal height is slightly underpredicted after 12 seconds, and for location C, the height is underpredicted between 10 and 40 seconds. These calculations assume a constant pour rate of 19.5 liters/min for the scale experiment which is consistent with the data reported in Reference 6. For gravity-driven injection vessels, the flowrate is initially higher than the average flow rate over the duration of the pour, and thereafter decreases due to decreasing gravity head in the injection vessel. This source of uncertainty may account for the descrepancy between the measured and predicted height transients at locations A and C during the early stages of the pour. Aside from the discrepancy in arrival times, the heights at locations D and E are reasonably predicted throughout the duration of the experiment. Note from Figure 9 the step behavior in the predicted heights at locations C and D. These steps correspond to the time at which the reflected hydraulic wave (which arises when the water fronts makes contact at the back of the annulus opposite the doorway) travels back to the location of the height sensors. For this run, the pour terminates at 62 seconds. Thereafter, the predicted behavior is a gradual equilibration of the heights to the equilibrium depth of 1.0 cm.

A comparison was also made with the experiment data obtained for Run No. 1. Reasonable agreement between the calculated and measured arrival times was obtained at all locations.

Examination of the observed spreading patterns reported for these experiments indicated that the spreading angle in the annulus just prior to shell contact could be less than the assumed value of 90°. In particular, for Run No. 2 at t = 5 seconds, the spreading angle was estimated as approximately 55°. In order to examine the sensitivity of the spreading behavior to the assumed value of the spreading angle, the calculation for Run No. 2 was repeated with the spreading angle set equal to 55°. The results of this calculation indicate that the height transients in-pedestal (Location A) and away from the doorway (Locations D and E) are insensitive to the choice of flow angle, whereas the transient height at Location C averages approximately 1 mm higher between 10 and 40 seconds when the smaller angle is assumed.

APPLICATION TO THE MK I SYSTEM

A scoping calculation was carried out to investigate the effects of melt freezing on the spreading potential and shell thermal loading in the full-scale Peach Bottom Mk I system geometry. Based on the considerations of Theofanous[6] for a station blackout sequence, a pour volume of 10 m^3 of mainly oxidic corium is assumed to drain under the influence of gravity through a localized breach in the reactor pressure vessel lower head at a constant flowrate of 3.25 m^3/min. Thirty percent of the zirconium inventory is assumed to have been oxidized at the time of vessel failure; the corresponding corium composition is 81 wt% UO_2, 8 wt% ZrO_2, and 11 wt% Zr. A decay heat level of 110 W/Kg UO_2 is assumed. The solidus and liquidus temperatures for the assumed corium mixture were estimated from the UO_2-ZrO_2-Zr tertiary phase diagram as 2170 K and 2670 K, respectively. Owing to the present level of uncertainty regarding corium spreading, it is not known whether immobilization of the spreading corium layer occurs when the layer temperature reaches the liquidus temperature, solidus temperature, or some intermediate temperature within the freezing range. The present approach is to make conservative assumptions which tend to maximize spreading potential, and therefore the corium is assumed to be immobilized when the temperature reaches the solidus value. Below the liquidus, the melt is modeled as a slurry with enhanced viscosity as predicted by Eq. (8). The slurry heat transfer is assumed to be the same as that with a pure liquid. The initial superheat temperature of the corium is assumed to equal 37 K relative to the liquidus temperature, which is consistent with the most probable superheat at vessel failure assumed in the analysis of Theofanous et al.[6] The pressure inside the drywell was assumed to equal 0.4 Megapascal absolute at the time of vessel meltthrough. A layer of water 0.45 meter deep and at 298 K temperature is assumed to be initially present in the drywell. The concrete substrate is assumed to be limestone aggregate-common sand concrete. Melt accumulation in the sump was ignored; melt is assumed to flow over the sump covers which do not melt through over the timescale of the calculation. The heat transfer coefficient between the melt and substrate is assumed to be given by a linear superposition of the forced convection and bubble agitation[13] heat transfer coefficients. The spreading angle between the pedestal doorway and shell is assumed to be 90°. The assumed nodalization for the Mk I calculations is illustrated in Figure 5.

The predicted transient height profiles at selected times are shown in Figure 10. Initial complete freezing of the corium layer is predicted to occur within the pedestal doorway, due to the large convective heat transfer associated with the acceleration of the melt through this flow constriction. Thereafter, the melt continues to accumulate as a slurry behind the solidified material, until the depth becomes sufficient for the melt to surge over the frozen debris. The relocating melt is in turn completely frozen, and the periodic melt surge and freezing process begins anew.

The disposition of molten corium and solidified debris one minute past the end of the pour is also shown in Figure 10. The melt is

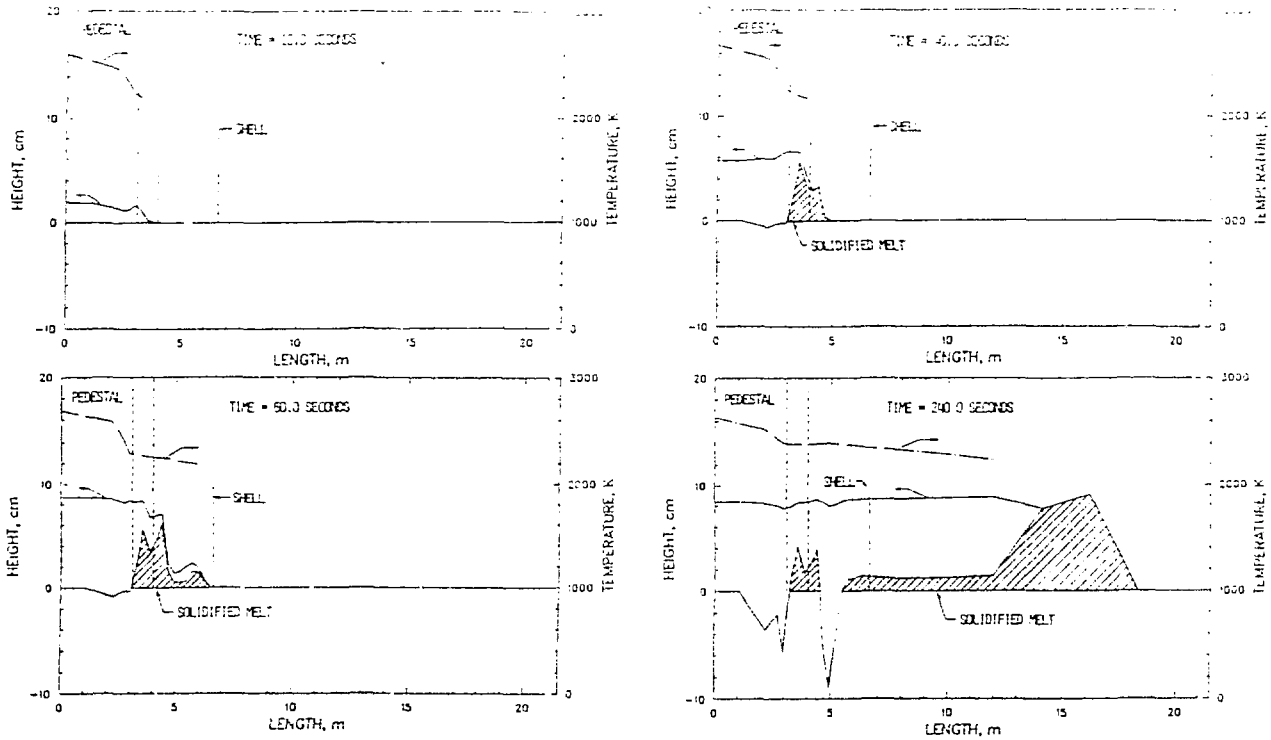

Figure 10. Predicted Transient Melt Height and Temperature Variations at Various Times for the Mk I System for the Case of UO_2-ZrO_2-Zr Corium, and the Corium is Immobilized at the Solidus Temperature.

predicted to cover approximately three quarters of the drywell annulus (approximately 270° subtended angle). This appears to be the limiting floor coverage at which heat transfer to overlying water and heat transfer to underlying steel (sump cover plates), ablating concrete, and solidified debris is able to remove the required energy to completely freeze the corium (initial leading edge solidification actually occurs at this location in the annulus at 130 seconds following pour inception). At this point, any additional melt which surges over the solidified leading edge is frozen at the leading edge, and the predicted behavior is a gradual accumulation of a "dam" at this location.

Although a significant amount of complete melt freezing is predicted to occur, the melt eventually propagates to the shell as a slurry at 62 seconds following pour inception. The calculated melt height and temperature adjacent to the shell are shown in Figure 11. Note that the melt temperature does not exceed the liquidus temperature over the calculated time interval. Thus, a less stringent melt immobilization criteria than that employed for this calculation (solidus temperaure) may well preclude melt propagation to the shell. The uncertainty in melt immobilization criteria points out the need for experiments using prototypic reactor materials with large characteristic freezing ranges in order to ascertain the correct melt immobilization characteristics.

The predicted shell surface temperature responses are shown in Figure 12. Initially, approximately 2 centimeters of corium is completely frozen immediately adjacent to the shell and the temperature behavior at the 0.5 cm

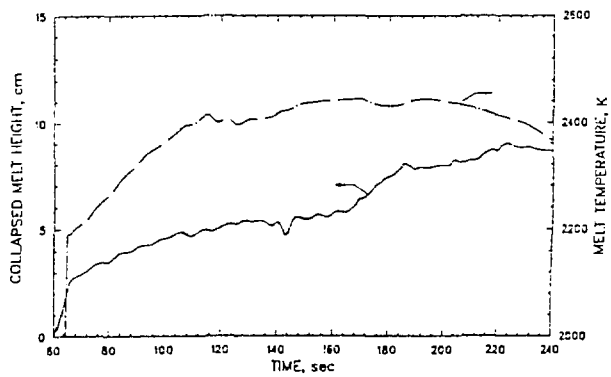

Figure 11. Predicted Melt Depth and Temperture Adjacent to the Shell for the Case of Melt Immobilization at the UO_2-ZrO_2-Zr Solidus Temperature.

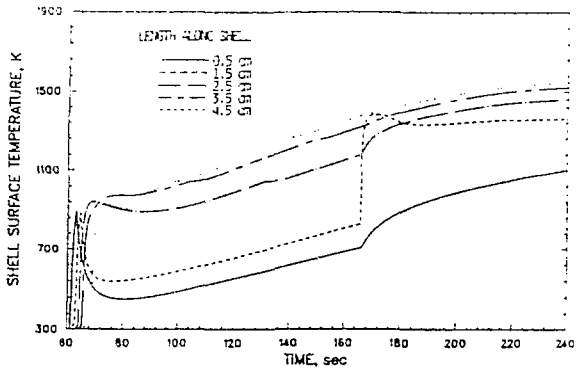

Figure 12. Predicted Shell Surface Temperature Response at Various Lengths Along the Shell for the Case of Melt Immobilization at the UO_2-ZrO_2-Zr Solidus Temperature.

and 1.5 cm elevations reflect the response due to transient conduction to solidified debris. A slurry of low temperature corium gradually accumulates over the frozen debris, however, and the surface temperature responses at the higher elevations reflect that characteristic of jet impingement heat transfer. A fairly uniform 5 mm thick crust is predicted to grow along the submerged portion of the shell. The inflection points in the shell temperature at the 0.5 cm and 1.5 cm elevations occurring at 160 seconds correspond to the point at which the debris adjacent to the shell has been remelted down to the 1.5 cm elevation. Note that the shell surface temperatures asymptotically approach a temperature of approximately 1500 K, which is below the melting temperature of 1810 K, but above the creep rupture temperature of about 1100 K at which the shell material undergoes a significant loss-of-strength and creep rupture becomes an important consideration.

In order to scope the effects of the freezing temperature range, the above calculation was repeated with liquidus and solidus temperatures characteristic of the UO_2-ZrO_2 binary system. For the assumed corium constituency, the solidus and liquidus temperatures were estimated from the phase diagram of Lambertson and Mueller[24] as $T_{solidus}$ = 2910 K and $T_{liquidus}$ = 2980 K. The initial melt superheat was again taken to be 37 K relative to the liquidus temperature.

The predicted transient melt height and temperature profiles at selected times are shown in Figure 13. Note that melt freezing is more pronounced for this case since the temperature difference driving the melt-to-water and melt-to-concrete heat transfer is greater. Initial freezing of the melt leading edge is predicted to occur just inside the pedestal doorway. The "dam" of solidified debris continues to accumulate leading to significant in-pedestal

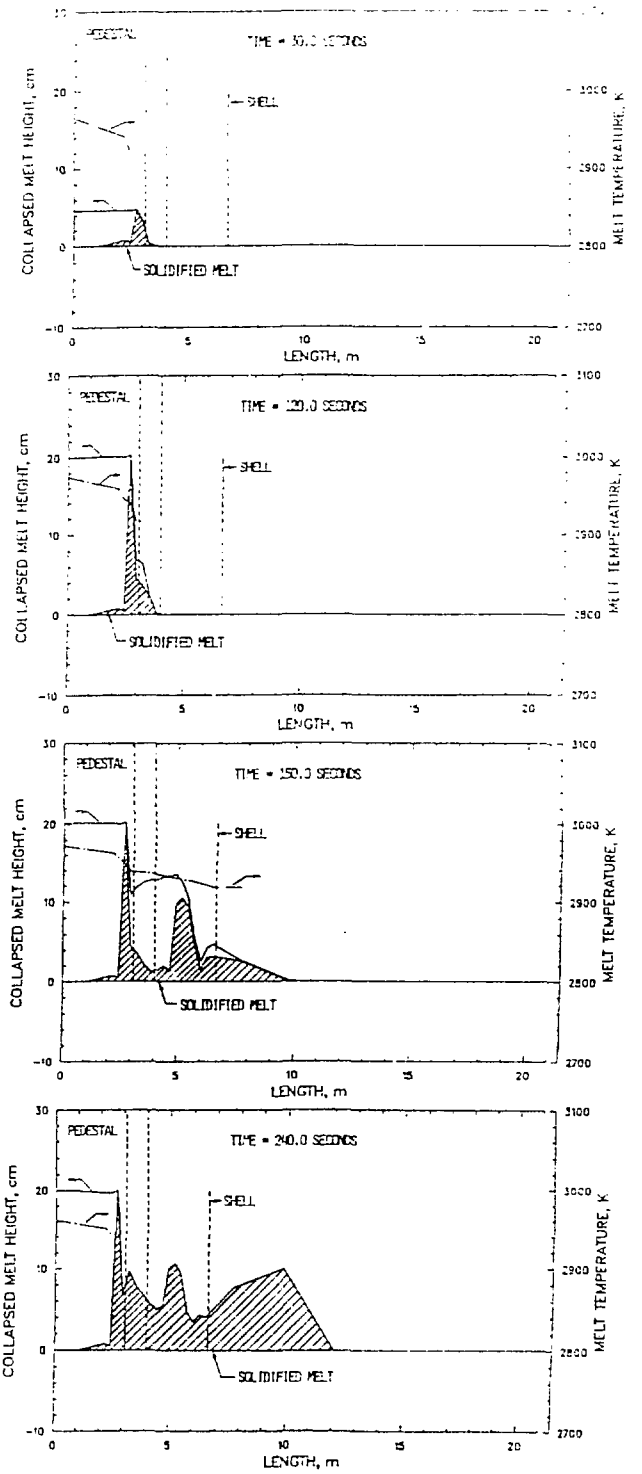

Figure 13. Predicted Transient Melt Height and Temperture Variations at Various Times for the Mk I System for the Case of Melt Immobilization at the UO_2-ZrO_2 Solidus Temperature.

retention of the melt, and delaying melt contact with the shell until 140 seconds after pour inception. The melt height and temperature adjacent to the shell are shown in Figure 14, while the corresponding shell temperature responses at various elevations along the shell are shown in Figure 15. A 5 centimeter deep layer of solidified debris is predicted to accumulate adjacent to the shell over the calculated time interval. Pour termination occurs at 184 seconds, and within 40 seconds following this time, the remaining molten corium outside the pedestal doorway is solidified. Examination of Figure 15 indicates that the peak shell surface temperature for this case is approximately 1040 K, which is below the creep rupture temperature of about 1100 K.

SUMMARY AND CONCLUSIONS

The MELTSPREAD-1 relocation model provides an integral computational capability for predicting melt relocation over the entire floor area of a Mk I containment. Comparison of model predictions with the water-simulant experiment data obtained by Theofanous et al.[6] in a 1/10 linear scale model of the Mk I containment indicates that the model reasonably predicts the arrival times and heights at selected locations within the pedestal and annular regions in the absence of freezing phenomena. A parametric calculation on the assumed flow angle in the region between the pedestal doorway and shell indicates that the predicted transient spreading behavior is insensitive to this variable.

The calculations for the Mk I reactor case indicate that with water present in the drywell, significant freezing of corium will occur between the pedestal doorway and the shell. Based on the conservative assumption that the corium is immobilized when the temperature reaches the solidus, the melt is predicted to reach the shell in the form of a slurry at 62 seconds past the start of the pour when the freezing temperature range for a UO_2-ZrO_2-Zr corium mixture is assumed. For a UO_2-ZrO_2 system, the corium reaches the shell as a slurry at 140 seconds. The peak shell surface temperature during the melt relocation phase is calculated to be 1540 K, for the UO_2-ZrO_2-Zr corium mixture which remains below the melting temperature for steel.

The results of these calculations emphasize the need for experiments using prototypic reactor materials in order to determine the appropriate melt immobilization behavior.

ACKNOWLEDGMENTS

This work was sponsored by the Electric Power Research Institute, Palo Alto, CA, under contract No. 3047-2. The authors are indebted to Dr. B. R. Sehgal, EPRI Project Manager, for his encouragement and support of this work. The authors are also indebted to prof. T. G. Theofanous, USCB, for interesting discussions on the Mk I issue and for providing additional information on the simulant experiments. The manuscript was prepared by L. J. Miller

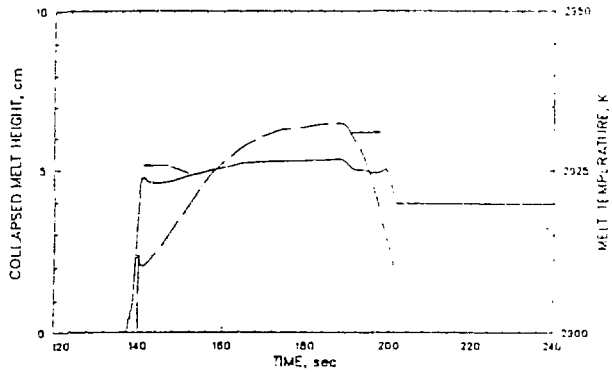

Figure 14. Predicted Melt Depth and Temperature Adjacent to the Shell Across from the Doorway for the Case of Melt Immobilization at the UO_2-ZrO_2 Solidus Temperature.

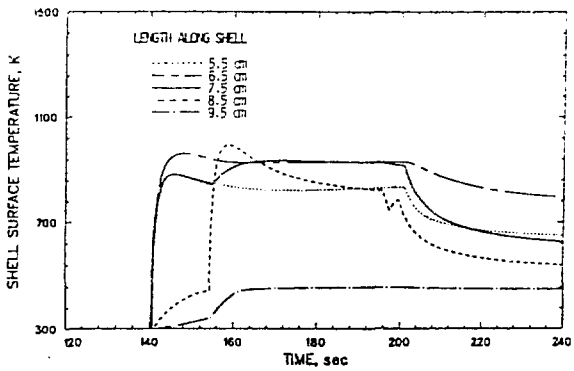

Figure 15. Predicted Shell Surface Temperature Response at Various Lengths Along the Shell for the Case of Melt Immobilization at the UO_2-ZrO_2 Solidus Temperature.

REFERENCES

1. G. A. Greene, K. R. Perkins, and S. A. Hodge, "Mark I Containment Drywell-Impact of Core/Concrete Interactions on Containment Integrity and Failure of the Drywell Liner," Source Term Evaluations for Accident Conditions-Preceedings of an International Symposium on Source Term Evaluation for Accident Conditions, Columbus, OH, October 28-November 1, 1985, pp. 429, International Atomic Energy Agency, Vienna (1986).

2. M. L. Corradini, "Current Status of LWR Containment Loads Due to Severe Reactor Accidents," Third International Topical Meeting on Nuclear Power Plant Thermal Hydraulics and Operations, Seoul, Korea, November 14-18, 1988.

3. M. S. Kazimi, "Recent Developments in Thermohydraulics of Severe Accidents," Third International Meeting on Nuclear Power Plant Thermal Hydraulics and Operations, Seoul, Korea, November 14-18, 1988.

4. G. A. Greene, "Discussion of the Technical Bases for Evaluation of the Vulnerability of the Mark I BWR Containment Shell to Melt-Through by Core Debris," U.S. NRC Mk I Containment Workshop, Baltimore, MD, February 24-26, 1988.

5. R. E. Henry, "Mk I Containment Experiments," U.S. NRC Mk I Containment Workshop, Baltimore, MD, February 24-26, 1988.

6. T. G. Theofanous, Private Communication, March 30, 1990.

7. J. J. Sienicki, M. T. Farmer, and B. W. Spencer, "Spreading of Molten Corium in Mk I Geometry Following Vessel Meltthrough," Fourth Proceedings Nuclear Thermal Hydraulics, Washington, D.C., October 30-November 4, 1988.

8. J. J. Sienicki, M. T. Farmer, and B. W. Spencer, " Spreading of Molten Corium in Mk I Geometry Following Vessel Melt-Through," Trans. Am. Nucl. Soc., Vol. 57, pp. 369-370 (1987).

9. H. Schlichting, Boundary Layer Theory, Fourth Edition, New York; McGraw-Hill, Inc., p. 525 (1960).

10. I. Kataoka and M. Ishii, "Prediction of Pool Void Fraction by New Drift Flux Correlation," NUREG/CR-4657, ANL-86-29, Argonne National Laboratory (June 1986).

11. J. K. Sherwood, R. L. Pigford, and C. R. Wilke, Mass Transfer, McGraw Hill, pp. 227 (1975).

12. M. Ishii and N. Zuber, "Drag Coefficient and Relative Velocity in Bubbly, Droplet, or Particulate Flows," AIChE Journal, Vol 25, pp. 843-855 (1979).

13. L. S. Kao and M. S. Kazimi, "Thermal Hydraulics of Core/Concrete Interaction in Severe LWR Accidents," MITNE-276, June 1987.

14. W. H. Rohsenow, "A Method of Correlating Heat Transfer Data for Surface Boiling of Liquids " Trans. ASME, Vol. 74, pp. 969-976 (1952).

15. N. Zuber, "On the Stability of Boiling Heat Transfer," Trans. ASME, Vol. 80, pp. 711-720 (1958).

16. H. J. Ivey and D. J. Morris, "On the Relevance of the Vapor-Liquid Exchange Mechanisms for Subcooled Boiling Heat Transfer at High Pressure," AEEW-R127 (1962).

17. M. T. Farmer, J. J. Sienicki, and B. W. Spencer, "CORQUENCH: A Model for Gas Sparging-Enhanced, Melt-Water, Film Boiling Heat Transfer," ANS Winter Meeting, Washington, D.C., November 11-15, 1990.

18. R. E. Henry, "A Correlation for the Minimum Film Boiling Temperature," AIChE Symp. Ser., Vol. 70, pp. 81-90 (1974).

19. J. J. Sienicki and B. W. Spencer, "Analysis of Reactor Material Experiments Investigating Corium Crust Stability and Heat Transfer in Jet Impingement Flow," ANL Proceedings 1985 National Heat Transfer Conference, Denver, CO, August 4-7, 1985, pp. 255, American Nuclear Society, LaGrange Park, IL (1985).

20. D. S. Jung, J. E. Venart, and A. C. Sousa, "Effects of Enhanced Surfaces and Surface Orientation on Nucleate and Film Boiling Heat Transfer in R-11," Int. J. Heat Mass Transfer, Vol. 30, pp. 2627-2639 (1987).

21. P. J. Berenson, "Film Boiling Heat Transfer From a Horizontal Surface," J. Heat Transfer, Vol. 83, pp. 351-357 (1961).

22. H. J. Sauer and S. C. Lin, "Effect of Inclination on Film Boiling," Proc. 5th Int. Heat Transfer Conf., Vol. 4, pp. 110-114 (1974).

23. T. B. Benjamin, "Gravity Currents and Related Phenomena," J. Fluid Mechanics, Vol. 31, Part 2, pp. 209-248 (1968).

24. W. A. Lambertson and M. H. Mueller, "Uranium Oxide Phase Equilibrium Systems: III, UO_2-ZrO_2," J. American Ceramic Society, Vol. 36, pp. 365 (1953).